Cao et al. *NPG Asia Materials* (2021) 13:1
https://doi.org/10.1038/s41427-020-00264-x

NPG Asia Materials

ARTICLE Open Access

Tailoring the *d*-band center of N-doped carbon nanotube arrays with Co_4N nanoparticles and single-atom Co for a superior hydrogen evolution reaction

Bo Cao[1], Minghao Hu[1], Yan Cheng[1], Peng Jing[1], Baocang Liu[1], Bo Zhou[2], Xi Wang[3], Rui Gao[1], Xiaolei Sun[4], Yaping Du[4] and Jun Zhang[1]

Abstract

A 3D self-supported integrated electrode, consisting of heteroatomic nitrogen-doped carbon nanotube arrays on carbon cloth with confined ultrafine Co_4N nanoparticles and a distribution of anchored single-atom Co, is fabricated via a cobalt-catalyzed growth strategy using dicyandiamide as the nitrogen and carbon source and a layered cobalt hydroxide-nitrate salt as the precursor. The abundance of exposed active sites, namely, the Co_4N nanoparticles, single-atom Co, and heteroatomic N-doped carbon nanotubes, and multiple synergistic effects among these components provide suitable tailoring of the *d*-band center for facilitating vectorial electron transfer and efficient electrocatalysis. Benefiting from the merits of its structural features and electronic configuration, the prepared electrode exhibits robust performance toward the hydrogen evolution reaction with overpotentials of only 78 and 86 mV at 10 mA cm^{-2} in acidic and basic electrolytes, respectively. Density functional theory calculations and X-ray photoelectron spectroscopy valence band measurements reveal that the effective tailoring of the *d*-band center by Co_4N nanoparticles plays a crucial role in optimizing the hydrogen adsorption free energy to a more thermoneutral value for efficient electrocatalysis.

Introduction

Impelled by the fast exhaustion of traditional fossil fuels and environmental stress, the request for clean renewable energy continues to increase every year[1]. Hydrogen, as an efficient, clean, and sustainable energy carrier, has become an ideal candidate to replace traditional fossil energy[2]. Electrochemical water splitting is identified as one of the most promising technologies for hydrogen generation. At present, great effort has been made to develop highly active electrocatalysts to decrease the overpotential and realize low-energy processes. To date, precious Pt-based materials are known as the most efficient electrocatalysts for the two half-reactions, named the hydrogen evolution reaction (HER)[3]. Nevertheless, the high cost and low reserve of these noble metal-based materials critically restrict their practical applications. Therefore, exploiting low-cost and earth-abundant electrocatalysts for the HER is of essential significance.

Currently, the development of superior electrocatalysts with earth-abundant elements for the HER has become a research priority. Among these studies, due to admirable electronic conductivity, vigorous stability, and environmental friendliness[4], many works are centralized on

Correspondence: Baocang Liu (cebcliu@imu.edu.cn) or Rui Gao (gaorui@imu.edu.cn) or Yaping Du (ypdu@nankai.edu.cn) or Jun Zhang (cejzhang@imu.edu.cn)
[1]School of Chemistry and Chemical Engineering, Inner Mongolia Key Lab of Nanoscience and Nanotechnology, Inner Mongolia Engineering and Technology Research Center for Catalytic Conversion and Utilization of Carbon Resource Molecules, Inner Mongolia University, Hohhot 010021, People's Republic of China
[2]Chemistry and Chemical Engineering Guangdong Laboratory, Shantou 515031, People's Republic of China
Full list of author information is available at the end of the article
These authors contributed equally: Bo Cao and Minghao Hu

carbon-based materials with various nanostructures, such as carbon nanotubes (CNTs)[5], carbon nanosheets[6], hollow carbons[7], and g-C_3N_4-based materials[8]. Commonly, heteroatoms such as N, P, B, and S are doped into carbon-based materials to optimize their electrocatalytic performances[9]. As ideal materials, CNTs and heteroatom-doped CNTs have received increasing attention in recent years due to their outstanding electrical conductivity, superior mechanical properties, large surface area, and strong coupling effect with active species[10]. Nonetheless, most of the CNTs used are commonly available in the form of powders[11], which is not only high-cost but also not convenient for making electrodes. Although chemical vapor deposition (CVD) techniques have been applied to directly grow CNTs on various substrates[10,12], some hazardous and environmentally unfriendly gases, such as CH_4 and H_2, are commonly used in these synthesis procedures, whose release is harmful to the environment. Additionally, the length and diameter of the CNTs are hard to control. Thus, developing a green and effective method to directly grow CNTs with a controllable length and diameter on various substrates and fabricate 3D self-standing CNT-based monolithic electrodes is highly desired; however, this development remains a challenge.

Transition metal-based materials, such as transition metal phosphides[13], sulfides[14], and carbides[15], have been reported as efficient electrocatalysts for the HER. However, these electrocatalysts generally suffer from poor stability. Interestingly, carbon-based materials are revealed to be effective for improving both the activity and durability of transition metal-based materials as protective shells. For example, it has been reported that when confining a CoNi alloy in a few layers of N-doped carbon (CoNi@NC), its electrocatalytic performance can be largely improved[4]. Moreover, when wrapping Co with N-doped CNTs and graphene (Co@N-CNT@rGO) to form a hybrid electrocatalyst, the electrocatalyst maintains very efficient catalytic activity ($-20\ mA\ cm^{-2}$ at a low overpotential) with long-term durability (100 h)[16]. According to a previous report, FeCo alloys confined in N-doped carbon shells in FeCo@N-CNT electrocatalysts can largely modify the electronic structure of the carbon surface, thus optimizing the performance for the HER[12]. However, when carbon shells become thicker, the effect of internal metal-based materials on the HER will be diminished[17].

It has been reported that the adsorption free energy of H (ΔG_{H^*}) is an appropriate parameter for evaluating the HER activity of a catalyst. In principle, an excellent HER electrocatalyst should have a ΔG_{H^*} close to zero, which can supply a quick proton/electron-transfer step and a quick hydrogen desorption process[18]. Previous reports have revealed that a downshifted *d*-band center can result in a suitable ΔG_{H^*} for the HER, thus optimizing the electrocatalytic activity of a catalyst toward the HER[19]. Co_4N, with Co–Co and covalent Co–N interactions, has been reported to be a promising electrocatalyst for the oxygen evolution reaction (OER)[20] because its *d*-band center is close to the energy level of the OER but far away from the energy level of the HER. To solve this problem, Wang's group handled the Co_4N for the HER by tailoring the *d*-band center with vanadium doping[19]. Additionally, it is also interesting to artificially tailor the intrinsic properties of carbon-based materials to achieve specific functions.

Herein, we successfully manipulated heteroatomic N-CNT arrays for efficient electrocatalytic HER by optimizing their *d*-band center with Co_4N nanoparticles confined in N-CNTs and single-atom Co anchored on N-CNTs. An effective cobalt-catalyzed growth strategy was developed to achieve N-CNT arrays on carbon cloth (CC) with internally confined Co_4N nanoparticles and externally anchored single-atom Co (Co_4N@CoSA/N-CNT/CC) using a newly developed layered cobalt hydroxide-nitrate salt (Co-LHS) as the catalyst and precursor and dicyandiamide (DCDA) as the nitrogen and carbon source for efficient HER electrocatalysis. The optimum Co_4N@CoSA/N-CNT/CC electrode shows remarkable HER performance compared with previously reported carbon-based electrocatalysts. It only requires 78 and 86 mV overpotentials to achieve $10\ mA\ cm^{-2}$ in 0.5 M H_2SO_4 and 1.0 M KOH solutions; furthermore, this electrocatalyst displays superior long-term stability with a small current loss after 5000 cyclic voltammetry (CV) cycles and no obvious decay after continual electrolysis for 50 h. Density functional theory (DFT) calculations reveal that the occurrence of the *d*-band center downshift, due to the effective regulation of the confined Co_4N nanoparticles, endows the Co_4N@CoSA/N-CNT/CC electrode with a feasible ΔG_{H^*} for efficiently catalyzing the HER. This work demonstrates a new idea for the fabrication of carbon-based electrodes and provides a promising approach for exploring novel HER electrocatalysts.

Results and discussion

As illustrated in Scheme 1a, a new type of lamellar cobalt precursor composed of layered Co-LHSs modified with ligand molecules of triethanolamine (TEOA) on the surface (Co-LHS@Co-TEOA) has been recently developed in our lab and possesses a similar structure as layered double hydroxides (LDHs). The lamellar cobalt precursor is primarily grown on CC under hydrothermal conditions in a mixture of $Co(NO_3)_2$ $6H_2O$ and TEOA aqueous solutions in the presence of pretreated CC. The as-formed Co-LHS@Co-TEOA precursor assembles into a 3D-hierarchical structure with uniformly oriented free-standing lamellar nanosheets according to SEM images (Supplementary Fig. S1a). Furthermore, its layered phase

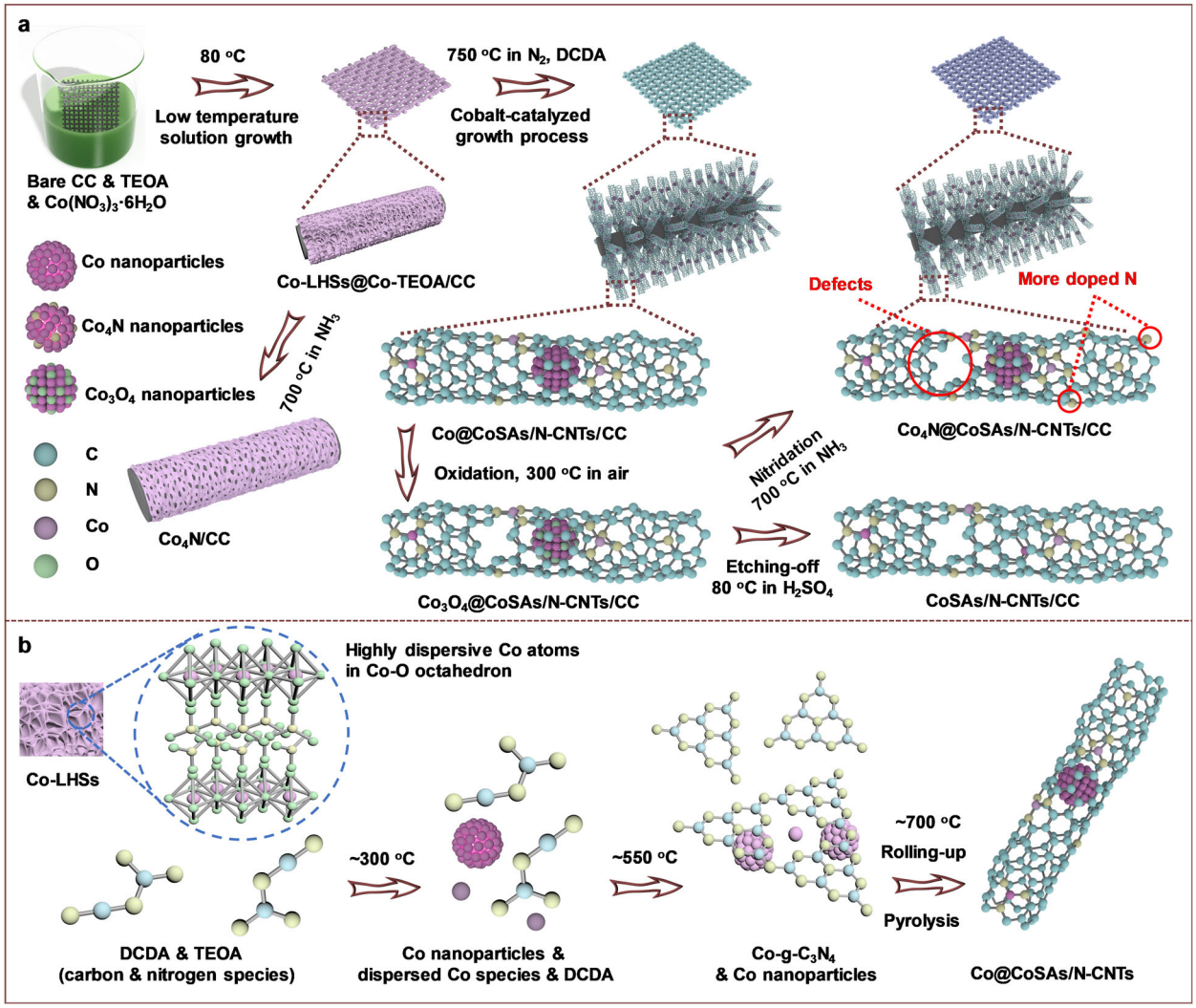

Scheme 1 a Schematic illustration showing the fabrication process of Co_4N@CoSA/N-CNT/CC. **b** Scheme showing the mechanism for the formation of single-atom Co. The lamellar cobalt precursor composed of layered cobalt hydroxide-nitrate salts (Co-LHSs) modified with ligand molecules of TEOA on the surface, which possesses a similar structure to that of layered double hydroxides (LDHs), is newly developed in our lab and plays a very important role in achieving high-quality Co_4N@CoSA/N-CNT/CC due to the well-controlled transformation of Co-LHSs into ultrafine Co nanoparticles embedded in N-CNTs and highly distributed single-atom Co anchored on N-CNTs.

structure, similar to previously reported transition metal-LHSs, was further confirmed by XRD characterization (Supplementary Fig. S1b). The coordinative modification of ligand molecules of TEOA is evidenced by IR measurements similar to a previous report[21]. The combined characterizations of thermogravimetric analysis, UV-vis absorption spectroscopy, and X-ray photoelectron spectroscopy (XPS), which will be addressed elsewhere, confirm that the Co-LHSs exists in the form of Co $(OH)_x(NO_3)_{2-x}{\cdot}mH_2O$ $(0 < x < 2)$. The well-defined lamellar cobalt precursor was then subjected to high-temperature treatment in a N_2 atmosphere in the presence of dicyandiamide as a carbon and nitrogen source. Under these treatment conditions, dicyandiamide can be easily catalyzed to grow well-defined N-CNTs in situ with heteroatomic N atom doping to form N-CNT arrays on CC. Then, this treatment induces the in situ transformation of Co-LHSs into ultrafine Co nanoparticles embedded in N-CNTs and highly dispersive Co single atoms anchored on N-CNTs (Co@CoSA/N-CNT/CC). After being immersed in acid to remove any excess oxidized Co species, the sample subsequently undergoes high-temperature nitridation in NH_3 to further transform the massive Co nanoparticles into Co_4N nanoparticles with the highly dispersed single-atom Co on the surface left unchanged; thus, Co_4N@CoSA/N-CNT/CC is successfully achieved. The loading mass of this electrode is approximately 3.2 mg cm^{-2}. The fabrication process can

be viewed visually according to the color changes of the CC substrate. The CC turns from gray to yellow after the initial hydrothermal treatment, then changes to black after the high-temperature treatment, and remains black after nitridation (Supplementary Fig. S2).

It is found that the high-quality lamellar cobalt precursor plays a crucial role in forming the 3D self-supported integrated Co_4N@CoSA/N-CNT/CC electrode. It not only acts as a cobalt and carbon source but also supplements the highly dispersed nucleation sites to ensure the formation of high-quality Co_4N nanoparticles and single-atom Co during the pyrolysis process at high temperature. This is confirmed based on a comparative study that when using traditional Co-LDHs as precursors and catalysts, only inferior quality and poorly dispersed Co@CoSA/N-CNT can be observed on CC (Supplementary Fig. S3), further revealing the importance of our Co-LHS precursors for synthesizing high-quality Co@CoSA/N-CNT arrays. Thus, the effectiveness and novelty of our synthesis strategy for rationally designing new CNT-based single-atom electrocatalysts is shown.

The possible formation mechanism for the CoSA/N-CNT array is displayed in Scheme 1b. During the synthesis process, Co–O octahedrons in Co-LHS precursors act as cages to accomplish the spatial separation and confinement of Co species, similar to the reported single atom-based (SA-based) materials using metal-organic frameworks as precursors[22]. At approximately 300 °C, the transformation from the Co-LHS precursor to Co nanoparticles and highly dispersed Co species occurs. Dicyandiamide is condensed into a melem species at 350 °C, resulting in the formation of g-C_3N_4 after further heating to approximately 550 °C. In this process, NH_3 gas is released from the breakdown of dicyandiamide and then further facilitates the atomization of Co and the doping of N in the carbon[22]. As the temperature is further increased to 750 °C, the presence of single-atom Co creates internal stresses and causes the layered Co-g-C_3N_4 to curl during the pyrolysis process at a high temperature, thus forming a cylindrical graphitic network of N-CNTs with confined Co_4N nanoparticles and anchored single-atom Co[22]. X-ray powder diffraction (XRD) was performed to determine the crystalline phase structure of the precursor and electrodes. All diffraction peaks of the precursor match well with the layered hexagonal Ni$(OH)_{1.6}(Ac)_{0.4}$·$0.63H_2O$ (ICDD PDF No. 56-0570) (Supplementary Fig. S1b), revealing that the obtained Co-LHS@Co-TEOA precursor is indeed composed of layered hydroxide cobalt salts (Co-LHSs) modified by ligand molecules of TEOA on the surface. As shown in Fig. 1a, the characteristic diffraction peaks of the original Co@CoSA/N-CNT/CC located at 44.2°, 51.5°, and 75.9° are attributed to the (111), (200), and (220) planes of the cubic metallic cobalt phase, respectively. After nitridation, diffraction peaks located at 43.7°, 50.8°, and 74.9°, corresponding to the (111), (200), and (220) planes of the cubic Co_4N phase, respectively[19], can be clearly observed, which reveals that the Co-LHS@Co-TEOA/CC and Co@CoSA/N-CNT/CC have been converted to Co_4N/CC and Co_4N@CoSA/N-CNT NA/CC electrodes, respectively. Additionally, the broad peak at 26.6° belonging to the characteristic peak of N-CNTs or CC can be found in both samples, indicating the presence of N-CNTs. Furthermore, the mean crystalline sizes of Co_4N nanoparticles are calculated to be ~22.3 and ~9.5 nm by the Scherrer equation based on the Co_4N(111) facet for Co_4N/CC and Co_4N@CoSA/N-CNT NA/CC, respectively, indicating that the size of the Co_4N nanoparticles is limited by CoSA/N-CNT.

Figure 1b presents the Raman spectra of the Co@CoSA/N-CNT/CC and Co_4N@CoSA/N-CNT/CC electrodes. Two peaks at approximately 1342.0 and 1585.0 cm^{-1}, representing the defects and disordered carbon (D-band) and sp^2 graphitic carbon (G-band), respectively, can be observed in Co@CoSA/N-CNT/CC and Co_4N@CoSA/N-CNT/CC. Three additional weak Raman peaks are detected at 468.4, 509.7, and 672.9 cm^{-1} in Co_4N/CC and Co_4N@CoSA/N-CNT/CC, which can be attributed to the meaningful contribution of the cobalt nitride phase[23]. Interestingly, the intensities of the D band to G band (I_D/I_G) of Co_4N@CoSA/N-CNT/CC are calculated to be 1.11, which is higher than the value of 0.96 for Co@CoSA/N-CNT/CC. This result implies that the oxidation and nitridation treatments can promote the defect density in CoSA/N-CNT caused by the anchored implementation of single-atom Co and N dopants in the carbon structure, which is widely believed to favor increasing the number of active sites for electrocatalytic water splitting[24].

To study the elemental composition and chemical bonding state, XPS was performed with Co_4N/CC, Co@CoSA/N-CNT/CC, and Co_4N@CoSA/N-CNT/CC. The XPS broad survey spectra (Fig. 1c) show that all three samples were composed of Co, O, N, and C without any other contaminants. In the Co 2p XPS spectrum of Co@CoSA/N-CNT/CC (Fig. 1d), multiple broad peaks can be observed, suggesting that Co should exist in more than one chemical state in Co@CoSA/N-CNT/CC[19]. After fitting the Co 2p spectrum, $Co^{\delta+}$ (778.5/793.5 eV), Co^{3+} (780.1/794.8 eV), and Co^{2+} (782.2/797.3 eV) peaks along with satellite peaks (786.4/803.2 eV) are identified[22], suggesting that the surface Co atoms have been partially oxidized to Co_3O_4. After nitridation, the characteristic XPS peaks of metallic Co and Co_3O_4 can also be found in the obtained Co_4N@CoSA/N-CNT/CC (Fig. 1d). The slightly positive shift in the binding energy of $Co^{\delta+}$ indicates the formation of Co_4N with weak Co–N bonds because of the similar atomic structure between Co_4N and closely packed metallic Co[25]. The existing Co^{3+} and Co^{2+}

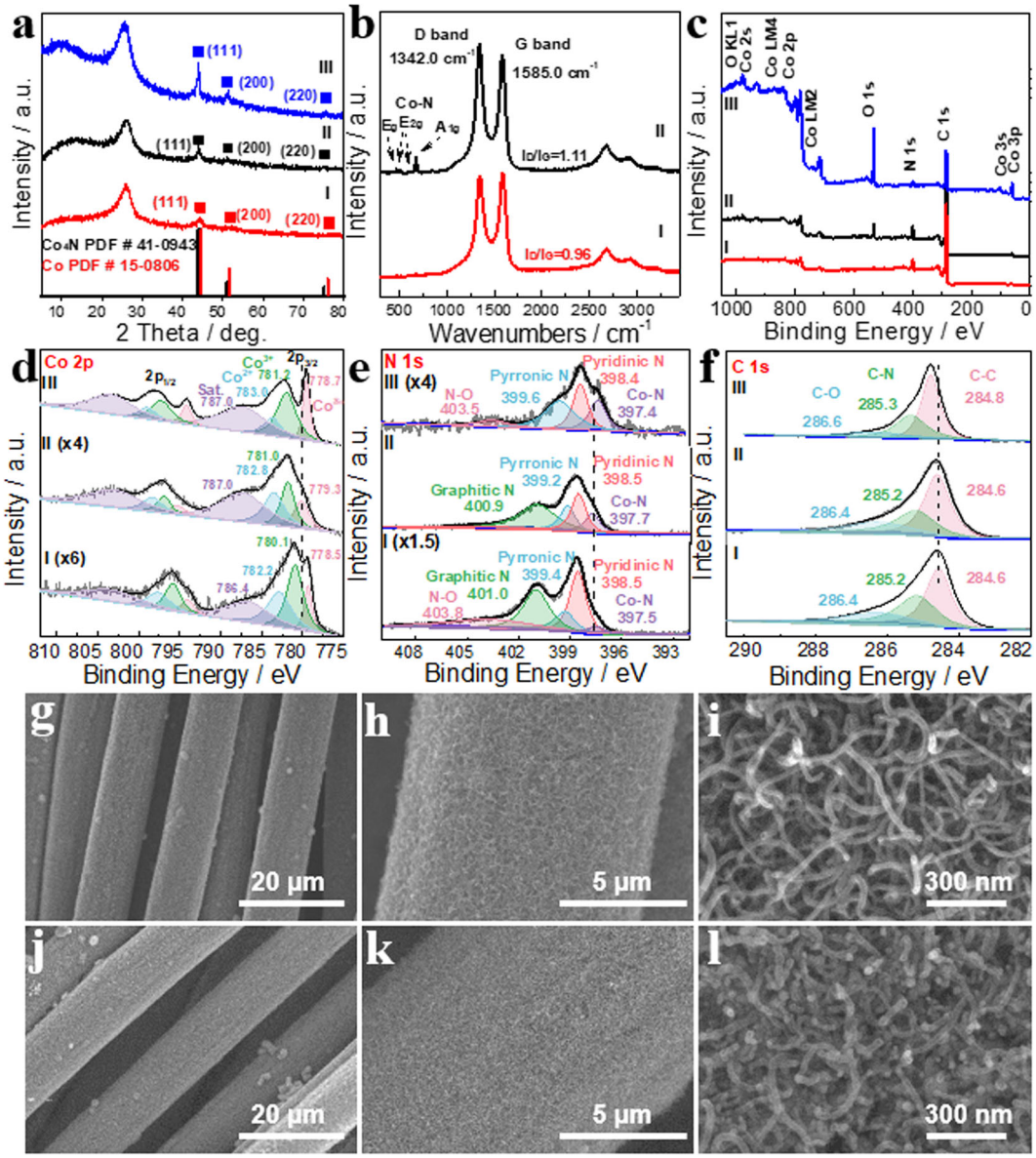

Fig. 1 XRD Patterns, Raman spectra, XPS spectra, and SEM images of these electrodes. a XRD patterns. **b** Raman spectra. **c** XPS broad survey spectra and core level spectra of: **d** Co 2p, **e** N 1s, and **f** C 1s of (I) Co@CoSA/N-CNT/CC, (II) Co_4N@CoSA/N-CNT/CC, and (III) Co_4N/CC. SEM images of **g**–**i** Co@CoSA/N-CNT/CC and **j**–**l** Co_4N@Co SAs/N-CNTs/CC.

peaks reveal that the surface of Co_4N is also partially oxidized. Moreover, a positive shift of the fitted $Co^{\delta+}$ peak can also be found in the Co_4N@CoSA/N-CNT/CC electrode compared to that of the Co_4N/CC electrode, demonstrating the occurrence of electrical coupling interactions in the electrode; this result may be due to the electron donation from Co_4N nanoparticles to CoSA/N-CNT, leading to electron-deficient Co_4N and electron-rich CoSA/N-CNT[26]. Clearly, the electronic regulation of CoSA/N-CNT and the interfacial synergy between metallic Co and CoSA/N-CNT can optimize the adsorption/desorption features of hydrogen/oxygen species, accordingly promoting the electrocatalytic properties of the material[4]. The N 1s XPS spectra of Co@CoSA/N-CNT/CC (Fig. 1e) can be split into five peaks at 397.7, 398.5, 399.4, 401.0, and 403.8 eV, which are assigned to Co–N bonds in carbon layers, pyridinic-N, pyrrolic-N, graphitic-N, and N-oxide, respectively. In regard to Co_4N@CoSA/N-CNT/CC, a strong peak is observed at 397.7 eV and corresponds to Co−N bonds in both carbon layers for single-atom Co and Co_4N nanoparticles[27], and this peak can also be observed in the N 1s XPS spectra of

Co_4N/CC at 397.4 eV. The shift in binding energies when comparing Co_4N/CC and Co_4N@CoSA/N-CNT/CC also provides evidence of an electronic interaction between Co_4N nanoparticles and CoSA/N-CNT, which is identical to the results from the Co 2p XPS spectra. The presence of abundant pyridinic-N and graphitic-N in CoSA/N-CNT may act as effective nonmetal active sites for the HER[16]. Furthermore, the binding energies of 284.6, 285.3, and 286.4 eV in the C 1s spectra of Co@CoSA/N-CNT/CC and Co_4N@CoSA/N-CNT/CC (Fig. 1f) are related to C–C, C–N, and C–O in CoSA/N-CNT[28]. Moreover, a peak belonging to the C–N bond can also be split in both samples, and such electronic interactions may change the electron density on carbon atoms and optimize the corresponding hydrogen adsorption Gibbs free energy (G_H^*), which is beneficial for promoting HER performance[29].

Scanning electron microscopy (SEM) was employed to further assess the morphology of different samples. As exhibited in Supplementary Fig. S1a, CC consists of cylindrical carbon fibers. After synthesis of the Co-LHS@Co-TEOA precursor, the cylindrical carbon fibers are fully covered by high-density lamellar Co-LHS@Co-TEOA nanosheets with a thickness of ~40 nm. SEM images of Co@CoSA/N-CNT/CC synthesized using different masses of dicyandiamide are shown in Supplementary Fig. S4. Interestingly, the diameter of CoSA/N-CNT decreases from 100 to 25 nm when the mass of dicyandiamide decreases from 0.6 to 0.2 g, implying that the diameter of N-CNTs is well regulated.

As a representative, the morphology and structure of Co@CoSA/N-CNT/CC synthesized using 0.2 g of dicyandiamide was studied in detail. As shown in Fig. 1g, h, each fiber in the CC is covered by uniform and dense CoSA/N-CNT arrays. The high-magnification SEM image (Fig. 1i) shows that the bent CoSA/N-CNT are ~1–2 μm in length and ~25 nm in diameter and have a smooth surface. The small diameter of CoSA/N-CNT can effectively restrict the growth of Co nanoparticles during the synthesis process, which is favorable for exposing more active sites and leads to enhanced electrocatalytic activity. After oxidation and nitridation, the tubular morphology of the high-quality Co@CoSA/N-CNT arrays is well maintained, except for the rough and porous surface (Fig. 1j–l). The unique CoSA/N-CNT structure can not only prevent the oxidation of confined Co_4N nanoparticles but also provide abundant nonmetal active sites on the CoSA/N-CNT surface via the coupling effect between Co_4N and CoSA/N-CNT[30], which largely promotes the activity and stability of the Co_4N@CoSA/N-CNT/CC electrode. The EDX elemental mapping images reveal the uniform distribution of Co, N, and C in Co_4N@CoSA/N-CNT/CC and Co@CoSA/N-CNT/CC (Supplementary Fig. S5), suggesting the successful incorporation of N in the CNTs and Co nanoparticles. The content of N in Co_4N@CoSA/N-CNT/CC is calculated to be 7.72 at.%, much higher than the 3.62 at.% in Co@CoSA/N-CNT/CC, revealing that more N atoms have been doped in Co@CoSA/N-CNT after nitridation in NH_3, which may provide more defective active sites in CoSA/N-CNT[31].

Transmission electron microscopy (TEM), high-resolution transmission electron microscopy (HRTEM), and high-angle annular dark-field scanning TEM (HAADF-STEM) measurements were obtained to reveal the microstructures of Co@CoSA/N-CNT and Co_4N@CoSA/N-CNT scratched off of the CC. In keeping with the SEM findings, the TEM images (Fig. 2a–g and Supplementary Figs. S6 and S7) of the Co@CoSA/N-CNT and Co_4N@CoSA/N-CNT reveal that ultrafine Co and Co_4N nanoparticles with a range from ~10 to 20 nm are encapsulated in situ by CoSA/N-CNT with a length of ~1–2 μm and a diameter of ~20 nm (Fig. 2a). In high-magnification TEM images (Fig. 2b, e), "bamboo joint-like" and multiwalled CoSA/N-CNT composed of N-doped graphitic carbon layers can be observed, in accordance with the as-reported metal-encapsulated carbon nanotubes[16]. Clearly, the sizes of Co and Co_4N nanoparticles match well with the diameter of CoSA/N-CNT, indicating the growth mechanism for the formation of CoSA/N-CNT as previously reported[16,32]. The HRTEM image of the Co@CoSA/N-CNT shows well-defined lattice fringes with interspacing distances of 0.340 and 0.204 nm, which can be attributed to the (002) and (111) lattice planes of graphitized carbon and metallic Co, respectively (Fig. 2b, c). Similarly, after nitridation in NH_3, the tubular structure is still well maintained (Fig. 2e), suggesting the outstanding thermal stability of CoSA/N-CNT. Moreover, approximately 8–10 intact layers of carbon in Co@CoSA/N-CNT can be observed (Fig. 2c), while only 3–5 layers of carbon with abundant defects are exhibited in Co_4N@CoSA/N-CNT (Fig. 2f). Previous studies have reported that a small number of layers and defects in carbon are beneficial to electronic transmission, thus resulting in remarkable activity for electrocatalysts[4,33]. Notably, a small number of carbon layers are found in Co_3O_4@CoSA/N-CNT (Supplementary Fig. S8), indicating that the decreases in the number of carbon layers and the generation of defects in CoSA/N-CNT are due to the oxidation process. The corresponding HRTEM image (Fig. 2f) shows fringe spacings of approximately 0.35 and 0.207 nm, assigned to the (002) and (111) lattice planes of graphitized carbon and Co_4N, respectively, indicating that the confined Co nanoparticles in CoSA/N-CNT are fully converted into Co_4N. HAADF-STEM images of Co_4N@CoSA/N-CNT exhibit some bright spots inside of N-CNTs, further suggesting the formation of CoSA/N-CNT with confined Co_4N nanoparticles (Fig. 2h, i). The corresponding EDX elemental mapping images show that the distributions of Co, N, and C are even in

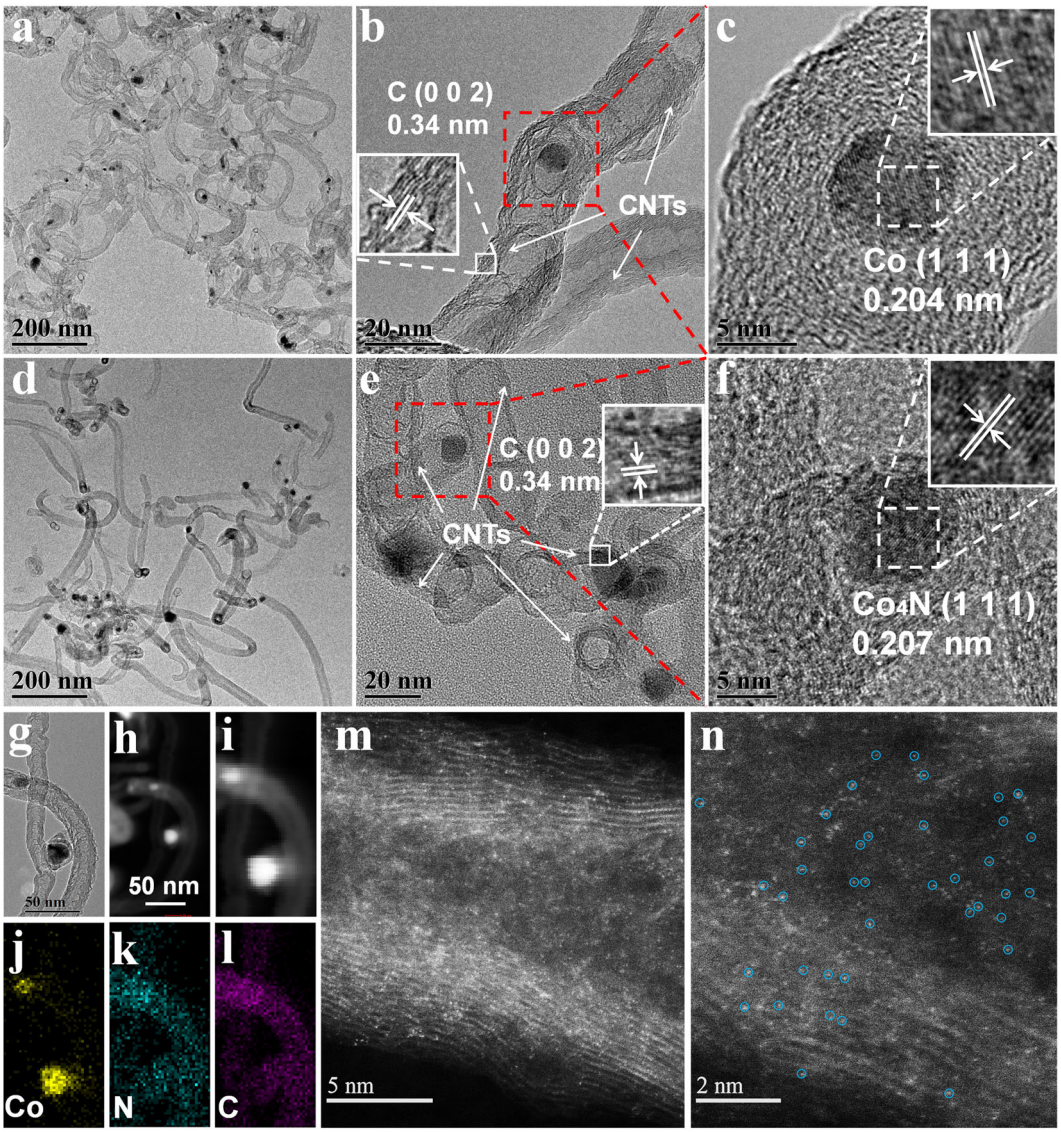

Fig. 2 TEM images, high-resolution TEM images of Co@CoSA/N-CNT and Co_4N@CoSA/N-CNT, and HAADF-STEM images of Co_4N@CoSA/N-CNT. a, **b** TEM images and **c** high-resolution TEM images of Co@CoSA/N-CNT. **d**, **e** and (**g**) TEM images, **f** high-resolution TEM images, **h**, **i** the corresponding HAADF-STEM, **j**–**l** elemental mappings, and **m**, **n** magnified HAADF-STEM image of Co_4N@CoSA/N-CNT.

N-CNTs, indicating the anchored single-atom Co in the N-doped CNT structure, while Co is mainly concentrated on the bright spots embedded inside N-CNTs (Fig. 2j–l). This result indicates that Co and N are uniformly doped in N-CNTs, which is consistent with the results obtained from SEM. Additionally, the contents of Co, N, and C in Co_4N@CoSA/N-CNT are calculated to be approximately 2.76, 3.72, and 93.52 at.%, respectively (Supplementary Fig. S7). To further elucidate the remaining single-atom Co, magnified aberration-corrected HAADF-STEM was carried out (Fig. 2m, n). To thoroughly study the components of N-CNTs, we dissolved Co nanoparticles in Co@CoSA/N-CNT after an oxidation process. XRD patterns and TEM images show that the Co nanoparticles have already completely dislodged (Supplementary Fig. S9). Nevertheless, the Co 2p XPS spectra exhibit the existence of Co species in N-CNTs, further illuminating that Co is doped in CoSA/N-CNT (Supplementary Fig. S10). Moreover, the EDX elemental mapping images and line-scan elemental distribution profiles display the enrichment of Co and N in the exterior of N-CNTs (Supplementary Fig. S11).

Stimulated by the unique structure and prospective composition, the electrocatalytic performance of the as-prepared Co_4N@CoSA/N-CNT/CC for the HER was assessed in a 0.5 M H_2SO_4 medium using a typical

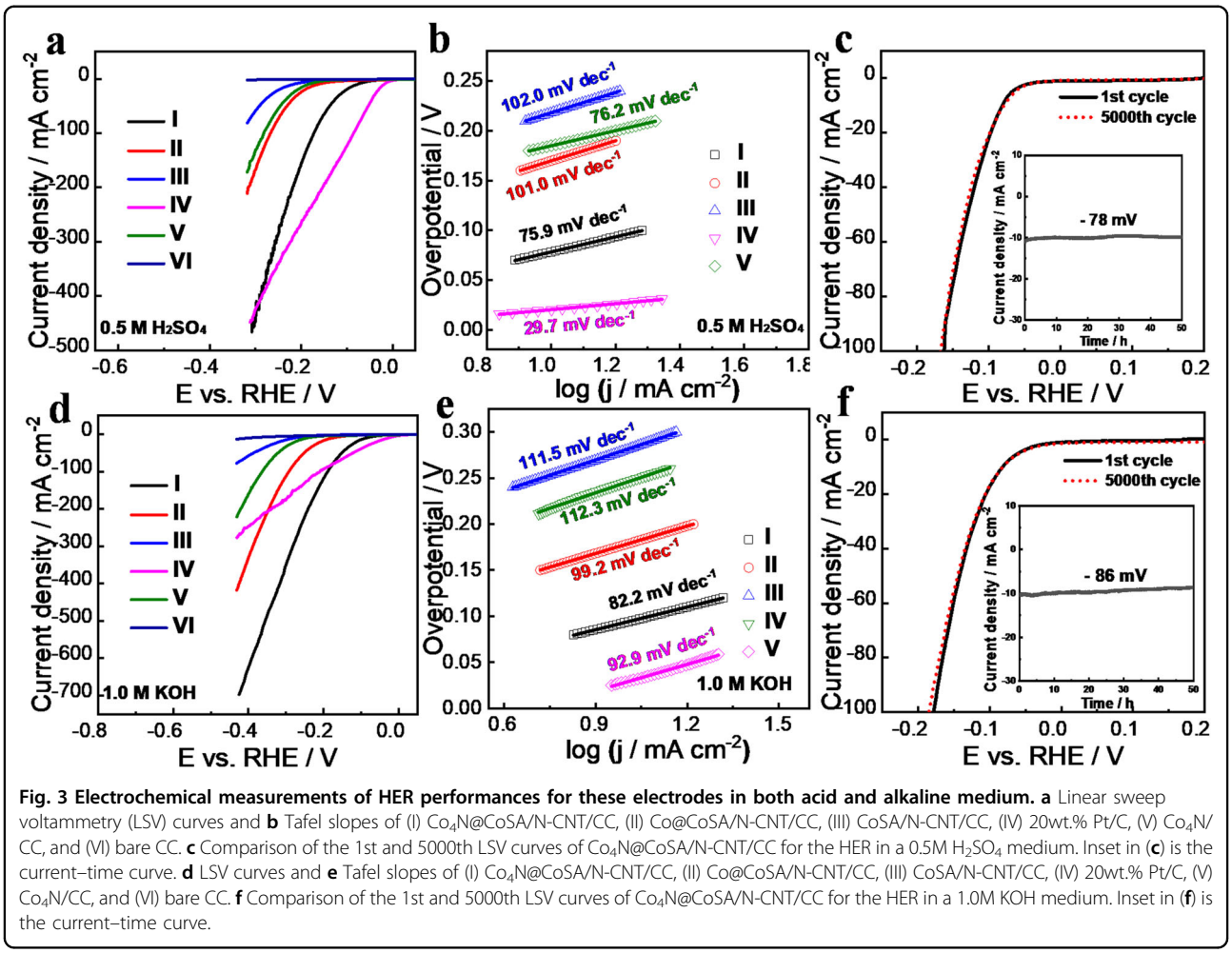

Fig. 3 Electrochemical measurements of HER performances for these electrodes in both acid and alkaline medium. a Linear sweep voltammetry (LSV) curves and **b** Tafel slopes of (I) Co_4N@CoSA/N-CNT/CC, (II) Co@CoSA/N-CNT/CC, (III) CoSA/N-CNT/CC, (IV) 20wt.% Pt/C, (V) Co_4N/CC, and (VI) bare CC. **c** Comparison of the 1st and 5000th LSV curves of Co_4N@CoSA/N-CNT/CC for the HER in a 0.5M H_2SO_4 medium. Inset in (**c**) is the current–time curve. **d** LSV curves and **e** Tafel slopes of (I) Co_4N@CoSA/N-CNT/CC, (II) Co@CoSA/N-CNT/CC, (III) CoSA/N-CNT/CC, (IV) 20wt.% Pt/C, (V) Co_4N/CC, and (VI) bare CC. **f** Comparison of the 1st and 5000th LSV curves of Co_4N@CoSA/N-CNT/CC for the HER in a 1.0M KOH medium. Inset in (**f**) is the current–time curve.

three-electrode setup at a scan rate of 2 mV s^{-1}. As a comparison, the HER activities of blank CC, benchmark 20 wt.% Pt/C, Co nanoparticle-free CoSA/N-CNT/CC, and Co@CoSA/N-CNT/CC were also studied. Figure 3a displays the polarization curves of these electrodes for the HER. To reflect the intrinsic electrocatalytic activities, 85% iR compensation was applied when obtaining the electrochemical measurements. As seen in Fig. 3a, 20 wt.% Pt/C displays an expected high HER activity with a near zero onset overpotential, while blank CC shows negligible HER activity. Notably, Co_4N@CoSA/N-CNT/CC requires a small overpotential of 78 mV to achieve a current density of −10 mA cm^{-2}, which is superior to blank CC (>300 mV), CoSA/N-CNT/CC (218 mV), Co_4N/CC (184 mV), and Co@CoSA/N-CNT/CC (164 mV), while also being 58 mV higher than 20 wt.% Pt/C. This result demonstrates that CoSA/N-CNT plays a vital role in promoting the electrocatalytic activity of Co_4N@CoSA/N-CNT/CC due to the strong coupling effect between Co_4N and CoSA/N-CNT[34]. The mechanism for the HER was further elucidated by the corresponding Tafel slopes. The Tafel slopes of CoSA/N-CNT/CC, Co@CoSA/N-CNT/CC, Co_4N@CoSA/N-CNT/CC, and Pt/C are fitted to be 102.0, 101.0, 75.9, and 29.7 mV dec^{-1} (Fig. 3b and Supplementary Table S1), respectively, suggesting that the corresponding HER over CoSA/N-CNT/CC, Co@CoSA/N-CNT/CC, and Co_4N@CoSA/N-CNT/CC abides by the same Volmer-Heyrovsky mechanism with the Volmer reaction as the rate-determining step[16,35]. Note that the Tafel slope is also a possible criterion to appraise the advantages of electrocatalysts, as a small Tafel slope signifies better scaling of the kinetics with voltages[16]. To further evaluate the catalytic kinetics and intrinsic properties for the HER of these electrocatalysts, the corresponding exchange current density (j_0) is determined by extrapolating the Tafel plots. Unexpectedly, j_0 of Co_4N@CoSA/N-CNT/CC is calculated to be 0.933 mA cm^{-2}, which is smaller than 2.090 mA cm^{-2} for 20 wt.% Pt/C but much higher than 0.209 mA cm^{-2} for Co@CoSA/N-CNT/CC and 0.073 mA cm^{-2} for CoSA/N-CNT/CC. The overpotential and exchange current density of Co_4N@CoSA/N-CNT/CC also outperform

most reported transition metal-based and CNT-based electrocatalysts. This result confirms the greatly enhanced catalytic activity of Co_4N@CoSA/N-CNT/CC compared with Co@CoSA/N-CNT/CC, Co_4N/CC, and CoSA/N-CNT/CC.

In addition to having high activity, the long-term durability is another crucial criterion to assess the superiority of an electrocatalyst. Thus, the stability of Co_4N@CoSA/N-CNT/CC was further examined by 5000 CV cycles and long-term current–time (*i*–*t*) tests at a fixed overpotential in a 0.5 M H_2SO_4 solution (Fig. 3c). After 5000 CV cycles, only an 8 mV increase in the overpotential can be observed at a current density of -100 mA cm^{-2}. In addition, the *i*–*t* curve obtained at a constant overpotential of 100 mV (insert of Fig. 3c) displays that the decrease in current density is only approximately 5% after continuous electrocatalysis for 50 h. Both results reveal that Co_4N@CoSA/N-CNT/CC possesses outstanding stability under acidic condition. The durability test results of Co_4N@CoSA/N-CNT/CC in the acidic medium are superior to that of other reported transition metal-based and CNT-based electrocatalysts. (Supplementary Table S3)

As reported, electrocatalysts with high activity and stability in alkaline medium are supposed to be of prime significance because most industrial technology utilizes alkaline electrolysis[16]. Hence, the HER activity of Co_4N@CoSA/N-CNT/CC was further investigated in an alkaline medium. Blank CC, benchmark 20 wt.% Pt/C, Co nanoparticle-free CoSA/N-CNT/CC, and Co@CoSA/N-CNT/CC were also studied under identical conditions for comparison. An 85% *iR* correction was also applied for these electrochemical measurements. As presented in Fig. 3d, Co_4N@CoSA/N-CNT/CC exhibits significant catalytic activity toward the HER in an alkaline medium, requiring overpotentials of only 86 and 189 mV to afford current densities of 10 and 100 mA cm^{-2}, respectively, which are far smaller than those of Co@CoSA/N-CNT/CC (178 and 292 mV), Co_4N/CC (244 and 363 mV), and CoSA/N-CNT/CC (280 mV at 10 mA cm^{-2}). Co_4N@CoSA/N-CNT/CC even catalyzes the HER in a manner that is comparable to that of commercial Pt/C at a high overpotential of 176 mV, further implying its superior HER activity. Likewise, the Tafel slopes were also determined on the basis of the Tafel equation. (Fig. 3e) In regard to Co_4N@CoSA/N-CNT/CC, the Tafel slope is calculated to be 82.2 mV dec^{-1}, superior to that of Co@CoSA/N-CNT/CC (99.2 mV dec^{-1}) and CoSA/N-CNT/CC (111.5 mV dec^{-1}). Additionally, the value of j_0 for Co_4N@CoSA/N-CNT/CC can reach 0.725 mA cm^{-2} in alkaline solution, approximately four times higher than that of Co@CoSA/N-CNT/CC (0.161 mA cm^{-2}) and nearly 20 times higher than that of CoSA/N-CNT/CC (0.030 mA cm^{-2}), further indicating more beneficial proton discharge kinetics for Co_4N@CoSA/N-CNT/CC. The HER performance of the Co_4N@CoSA/N-CNT/CC electrode is also higher than that of most currently reported transition metal-based and CNT-based electrocatalysts in alkaline media (Supplementary Table S4). Notably, Co_4N@CoSA/N-CNT/CC also exhibits superior long-term stability in the alkaline medium. As shown in Fig. 3f, upon accelerating durability tests (ADTs) with the use of 5000 continuous cycles, Co_4N@CoSA/N-CNT/CC only shows a slight overpotential increase of 14 mV at a current density of -100 mA cm^{-2}. Furthermore, when a static overpotential of 86 mV is applied, the current density of Co_4N@CoSA/N-CNT/CC can be maintained at 89% after long-term stable electrolysis for more than 50 h (inset of Fig. 3f), which is also superior to reported transition metal-based and CNT-based electrocatalysts. (Supplementary Table S5). As shown in Supplementary Fig. S12, after long-term durability testing, the morphology of Co_4N@CoSA/N-CNT/CC remains good. The chemical composition of the electrode used in the acidic medium remains unchanged, while some Co_4N nanoparticles transfer to $Co(OH)_2$ after the stability test in the alkaline medium. These results show that the Co_4N@CoSA/N-CNT/CC electrode is stable during long-term operation in both acidic and alkaline media.

To reveal the electrode kinetics for Co_4N@CoSA/N-CNT/CC and Co@CoSA/N-CNT/CC, electrochemical impedance spectroscopy (EIS) measurements were conducted at different overpotentials in 0.5 M H_2SO_4 and 1.0 M KOH solutions. The Nyquist plots of different electrodes in 0.5 M H_2SO_4 and 1.0 M KOH electrolytes show that the HER can be accelerated along with increasing overpotentials (Supplementary Figs. S13 and S14), which suggests one-time constant behavior for the electrode during the HER process (Supplementary Fig. S15). One-time constant behavior contains a resistor and one parallel circuit, where R_s, R_{ct}, and C_{dl} represent the solution resistance, charge-transfer resistance, and constant phase element, respectively. The Nyquist plots of the experimental and fitted data for different electrodes at overpotentials of 150 mV by a one-time constant model are also provided (Supplementary Fig. S16a, b), and the obtained R_s and R_{ct} are listed in Supplementary Table S6. As expected, the Co_4N@CoSA/N-CNT/CC electrode exhibits small charge-transfer resistances of 12.67 and 13.26 Ω at the electrode/electrolyte interface for the HER in acidic and alkaline electrolytes, lower than those of Co@CoSA/N-CNT (24.85 and 26.72 Ω) and CoSA/N-CNT/CC (65.06 and 67.30 Ω) electrodes, indicating that it follows rapid charge transfer kinetics for electrocatalytic reactions[36]. The superior electron-charge transfer property can promote the combination of electrons and H_{ads}, and benefit the reduction of ohmic losses[37], hence resulting in the improvement in electrocatalytic activity.

The effective electrochemical active surface areas (ECSAs), revealing the number of active sites, can be estimated from the corresponding double-layer capacitance (C_{dl}), which is proportional to the ECSAs. Thus, the values of C_{dl} for Co_4N@CoSA/N-CNT/CC and Co@CoSA/N-CNT/CC were measured by CV at various scan rates within the non-Faradaic potential range of 0.1–0.3 V vs. reversible hydrogen electrode (RHE) (Supplementary Fig. S16c, d). As a result, the C_{dl} is calculated to be 49.50 mF cm^{-2} for Co_4N@CoSA/N-CNT/CC, which is only half of the C_{dl} of Co@CoSA/N-CNT/CC (105.12 mF cm^{-2}, Supplementary Fig. S16e), suggesting a small number of active sites for Co_4N@CoSA/N-CNT/CC. After being normalized by C_{dl}, the electrocatalytic activity of each active site in Co_4N@CoSA/N-CNT/CC, e.g., the intrinsic electrocatalytic activity, is far higher than that of Co@CoSA/N-CNT/CC, which further indicates the superior electrocatalytic activity of Co_4N@CoSA/N-CNT/CC.

The efficient electrocatalytic performance of the Co_4N@CoSA/N-CNT/CC electrode is mainly attributed to its unique structure and configuration. First, as metallic active sites, small Co_4N nanoparticles with a diameter of ~10–20 nm encapsulated in CoSA/N-CNT can be easily exposed to electrolytes from the defects of CoSA/N-CNT, which offer more exposed catalytically active sites. Second, the unique 3D open structure of CoSA/N-CNT arrays supplies a high interfacial contact area with the electrolyte, which is favorable for diminishing the resistance of ion diffusion and charge transfer[38]. Third, the synergistic effect between CoSA/N-CNT and Co_4N nanoparticles can not only efficiently boost the electron transfer ability and decrease the interfacial charge-transfer resistance but also offer the opportunity to tune intrinsic electronic properties and produce abundant nonmetallic active sites on CoSA/N-CNT[12]. These structural merits are also beneficial for improving electrocatalytic performance[39].

DFT calculations were employed to gain insight into the high HER activity of the Co_4N@CoSA/N-CNT/CC electrode. On the basis of the experimental results of HRTEM (Fig. 2c, f) and XPS (Fig. 1e), catalyst models of the bare Co_4N(111) and Co(111) unit cells, as well as the two surfaces encapsulated in a carbon shell (@C) and nitrogen-doped carbon shell (@NC), are constructed and shown in Supplementary Figs. S17 and S18. As exhibited in Fig. 4a, the computational results show that Co_4N and Co provide large exothermic ΔG_{H^*} values of −0.58 and −0.39 eV, respectively, revealing the poor HER activities of bare Co_4N and Co caused by the predictable difficulty of hydrogen release. After encapsulation with the C shell (@C) and N-doped C shell (@NC), the obtained Co_4N@C and Co_4N@NC display ΔG_{H^*} values of +0.16 and −0.12 eV, much closer to zero than those of Co@C (+ 0.40 eV), Co@NC (+ 0.24 eV), and the bare slab. Clearly, the ΔG_{H^*} value of Co_4N@NC is closest to zero among these models, suggesting that Co_4N@NC possesses optimal intrinsic HER activity, which matches well with the experimental results.

Subsequently, to deeply understand the optimal intrinsic activity of the HER, the *d*-band centers, Bader charges, and charge differences of Co, bare Co_4N, Co@C, Co@NC, Co_4N@C, and Co_4N@NC were computed. As shown in Fig. 4b, all three *d*-band centers of metallic Co in the Co_4N electrocatalyst models (−1.280 ~ −1.392 eV) are far from the Fermi level than those in the corresponding Co models (−1.168 ~ −1.229 eV), and the tailoring of *d*-band centers leads to a lower desorption energy of H[19,40]. The adsorption behavior of the Co_4N@CoSA/N-CNT/CC and Co@CoSA/N-CNT/CC electrodes was further evaluated by XPS valence band measurements (Supplementary Fig. S19). With respect to the Fermi level, the derived *d*-band centers exhibit a tailored trend from Co@CoSA/N-CNT/CC (−1.59 eV) to Co_4N@CoSA/N-CNT/CC (−1.80 eV), which corresponds well with the DFT calculation results.

Moreover, it can be clearly found that the order of the three *d*-band centers in the Co_4N electrocatalyst models (Co_4N@NC < Co_4N@C < Co_4N) is coincident with the energy level of the absolute value of ΔG_{H^*}, i.e., the low *d*-band center in the Co_4N models exhibits weak absorbability and high HER activity. For comparison, between the *d*-band center and ΔG_{H^*}, a similar relationship can also be found in the corresponding Co models. Moreover, the Bader charges (Supplementary Table S7) of the different elements in the H-Co, H-Co_4N, H-Co@C, H-Co_4N@C, H-Co@NC, and H-Co_4N@NC structures as well as the corresponding charge density differences (Fig. 4c-f) of the @C and @NC shells are calculated. In Supplementary Table S7, all the Bader charges of the metallic Co atoms are negative, while the Bader charges of the nonmetallic N and C atoms are positive in both the Co slab, Co_4N slab, carbon layer, and N-doped carbon layer, indicating that electrons will be transferred from Co to C and N, which is in good agreement with the XPS results. In Fig. 4c-f, the analysis of charge density differences also shows the same conclusion as the Bader charges. The electron transfer from Co_4N nanoparticles to the carbon atoms in N-CNTs then further to the nitrogen atoms, along with the electron transfer from single-atom Co to nitrogen atoms, leads to the Co_4N nanoparticles and single-atom Co being electron-deficient regions, while N-CNTs are electron-rich regions. In this regard, electronic coupling results in electron-rich N-CNTs with a decrease in the *d*-band center of the electrode; thus, the energy level of the antibonding states is lowered and easily filled, leading to the low-desorption energy of H in the HER[26,40].

Moreover, considering the synergistic effect of single-atom Co in N-CNTs, electrocatalyst models of

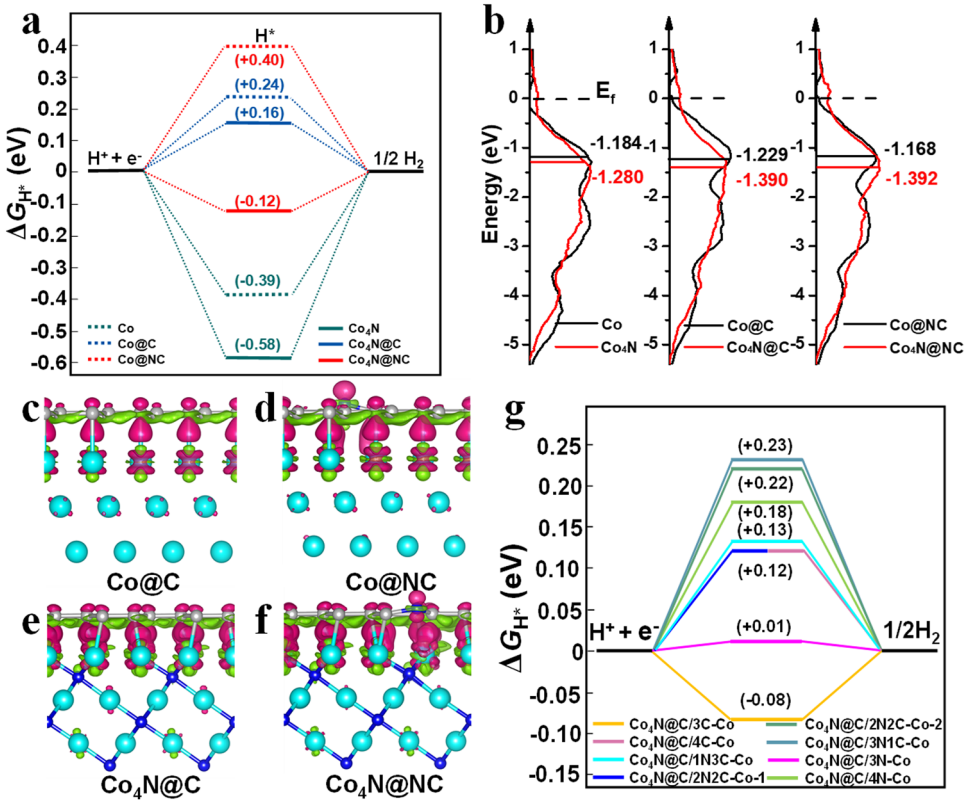

Fig. 4 DFT calculations of HER on several electrocatalysts. a Free-energy diagram of the HER on various Co and Co_4N catalysts, **b** partial electronic density of states (PDOS) for the d orbital of bare Co, bare Co_4N, Co@C, Co_4N@C, Co@NC, and Co_4N@NC. The dotted lines represent the Fermi level, and the *d*-band centers of Co atoms are provided with the colored font. Charge density differences of the N-doped carbon layer in the models of: **c** Co_4N@C, **d** Co@NC, **e** Co@NC, and **f** Co_4N@NC. In the structures of (**c**–**f**), Co, N, and C are marked in cyan, blue, and gray, respectively. In regard to the charge density differences, red and green represent charge accumulation and depletion, respectively. The isosurface cutoff is 0.005 electrons$Å^{-3}$. **g** Free-energy diagram of the HER at various single-atom Co sites of the Co_4N@CoSA/N-CNT/CC electrocatalyst.

Co_4N@C/xNyC-Co unit cells are constructed and shown in Supplementary Fig. S20. As exhibited in Fig. 4g, the computational results show that all single-atom Co sites provide a small absolute value of ΔG_{H^*}, less than 0.23 eV. Among these, Co_4N@C/3N-Co exhibits the optimal value of 0.01 eV. These results reveal the crucial role of single-atom Co in Co_4N@CoSA/N-CNT/CC for the HER. In total, the electronic property analysis demonstrates that the doping of nonmetallic nitrogen can tune the electron density of the carbon layer and the *d*-band center of the Co_4N slab. This result leads to the optimal HER activity of Co_4N@CoSA/N-CNT/CC.

Conclusions

In summary, we reported the fabrication of a novel 3D self-supported integrated electrode composed of well-defined heteroatomic N-doped carbon nanotube (N-CNT) arrays on CC with simultaneously confined Co_4N nanoparticles in situ inside N-CNTs and anchored single-atom Co on the N-CNT walls (Co_4N@CoSA/N-CNT/CC) for excellent HER electrocatalysis. The novel Co_4N@CoSA/N-CNT/CC electrode possesses a uniform 3D-hierarchical structure with highly accessible active sites exposed due to the Co_4N nanoparticles, single-atom Co, and N-CNTs, which promote the significant improvement in catalytic performance. Moreover, the strong multiple synergistic effects among the Co_4N nanoparticles, single-atom Co, and N-CNTs provide the suitable tailoring of the *d*-band center and the effective regulation of the electronic configuration for efficient electrocatalysis. Thus, the Co_4N@CoSA/N-CNT/CC electrode exhibits excellent electrocatalytic performance and only needs overpotentials of 78 and 86 mV to achieve a current density of 10 mA cm^{-2} for the HER in 0.5 M H_2SO_4 and 1.0 M KOH solutions, respectively. More importantly, such an electrode also displays superior long-term stability with a small current loss after 5000 CV cycles and no obvious decay after continual electrolysis for 50 h. Further DFT calculations reveal that the *d*-band center of the electrocatalyst can be tailored by the confined Co_4N

nanoparticles in the N-CNTs and anchored single-atom Co to endow Co_4N@CoSA/N-CNT/CC with an applicable ΔG_{H^*} value for the HER. Our work develops a convenient and efficient approach for constructing 3D self-supported CNT-based monolithic electrodes.

Materials and methods

Materials

$Co(NO_3)_2{\cdot}6H_2O$, HNO_3 (68 wt%), and H_2SO_4 (98 wt%) were purchased from Beijing Chemical Works (Beijing, China). KOH was purchased from Aladdin Ltd. (Shanghai, China). CC was purchased from Innochem Science & Technology Co., Ltd. (Beijing, China). Platinum, nominally 20% carbon black, IrO_2, and dicyandiamide (DCDA) were purchased from Alfa Aesar (Shanghai, China). TEOA and ethanol were purchased from Sinopharm Chemical Reagent Co., Ltd. (Beijing, China) All reagents were used as received without further purification.

Materials characterization

XRD was performed on a PANalytical Empyrean diffractometer with a Cu K alpha1 radiation source ($\lambda = 1.5405$ Å) operated at a scanning rate of 0.013° at Bragg angles ranging between 5° and 80°. Transmission electron microscopy (TEM) and scanning transmission electron microscopy (STEM) characterizations were performed on an FEI Tecnai F20 field-emission transmission electron microscope (FE-TEM) and a JEOL ARM200F 200 kV STEM, respectively. Scanning electron micrographs were recorded by field-emission scanning electron microscopy (FE-SEM, Hitachi S-4800). XPS measurements were performed with a VG Scientific ESCALAB Mark II spectrometer equipped with two ultrahigh vacuum (UHV) chambers. All spectra were calibrated with the C–C peak of C 1s orbitals as 284.6 eV. Raman spectroscopy characterizations were carried out using a Renishaw inVia Raman microscope with a 532 nm laser source under vacuum conditions in an in situ reaction cell.

Synthesis of the Co-LHSs/CC precursors

All chemicals used in the experiments were analytical grade and used as received without further purification. Prior to the hydrothermal treatment, CC was first cut into small pieces with a size of 2 × 3 cm, cleaned by being placed in boiling concentrated nitric acid for 12 h at 80 °C, washed sequentially with water, acetone, and ethanol, and finally dried at 60 °C for 10 min. To synthesize Co-LHS precursors, $Co(NO_3)_2{\cdot}6H_2O$ (0.7 mmol) was dissolved in a mixed solvent consisting of 25 mL of deionized water and 5 mL of TEOA in a 50 mL autoclave, and the clean CC (2 × 3 cm) was then immersed in the resultant solution. This reaction system was then kept at 80 °C for 24 h. After cooling to room temperature, the as-obtained Co-LHSs/CC precursors were washed with deionized water three times and dried at 60 °C.

Synthesis of Co@CoSA/N-CNT/CC

Co-LHS/CC precursors were placed in a quartz boat with dicyandiamide at the upstream side of the furnace. Then, the samples were heated to 450 °C for 2 h at a heating rate of 2 °C min^{-1} to sufficiently deposit dicyandiamide on the surface of the Co-LHS/CC and then heated to 750 °C for 2 h at a heating rate of 2 °C min^{-1} in a N_2 atmosphere. After cooling to room temperature, Co@CoSA/N-CNT/CC was obtained. To adjust the diameter of the N-CNTs, 0.2, 0.4, and 0.6 g dicyandiamide were used to fabricate different Co@CoSA/N-CNT/CC electrodes.

Synthesis of Co_3O_4@CoSA/N-CNT/CC

Co@CoSA/N-CNT/CC were placed in a quartz boat, and the samples were heated to 300 °C for 2 h at a heating rate of 2 °C min^{-1} in an air atmosphere. After cooling to room temperature, Co_3O_4@CoSA/N-CNT/CC was obtained.

Synthesis of Co_4N@CoSA/N-CNT/CC

Co_3O_4@CoSA/N-CNT/CC were placed in a quartz boat, and the samples were heated to 750 °C for 3 h at a heating rate of 2 °C min^{-1} in an NH_3 atmosphere. After cooling to room temperature, Co_4N@CoSA/N-CNT/CC was obtained.

Synthesis of CoSA/N-CNT/CC

Co_3O_4@CoSA/N-CNT/CC was placed in boiling H_2SO_4 for 12 h at 80 °C and washed with deionized water several times.

Electrochemical measurements

Electrochemical measurements were carried out on a Zennium electrochemical workstation (Zahner, Germany) assembled with a standard three-electrode system with a carbon rod electrode as the counter electrode, the prepared integral electrodes as the working electrode, and a saturated calomel electrode (SCE, 0.241 V vs. RHE) as the reference electrode. All potentials were referenced to a RHE by adding a value of $(0.241 + 0.059 \times pH)$ V. Linear sweep voltammetry (LSV) polarization curves in the potential range of −0.6 to 0 V (vs. SCE) for the HER were acquired in N_2-saturated 0.5 M H_2SO_4, and in the potential range of −1.5 to −0.8 V (vs. SCE) for the HER acquired in N_2-saturated 1.0 M KOH. LSV tests were performed at a scan rate of 2 mV s^{-1}. Before each activity measurement, the electrodes were pretreated by CV in the potential range of the LSV test at a sweep rate of 100 mV s^{-1} for at least 50 cycles without rotation to activate the catalysts, remove surface contamination, and stabilize the

current. The ADTs were conducted by performing up to 5000 CV cycles in a 0.5 M H_2SO_4 electrolyte in the potential range of −0.4 to 0 V (vs. SCE) and 5000 CV cycles in a 1.0 M KOH electrolyte in the potential range of −1.4 to −1.0 V (vs. SCE) for the HER. The amperometric current density–time (*i*–*t*) curves were measured for 50 h in N_2-saturated 0.5 M H_2SO_4 and1.0 M KOH solutions under controlled potentials. The electroactive surface areas were measured by a series of CV measurements performed from 0.1 to 0.3 V versus the RHE at various scan rates ranging from 20 to 180 mV s^{-1}, and 20 continuous sweep cycles were performed to ensure consistency. EIS measurements were carried out from 100,000 to 0.04 Hz in 0.5 M H_2SO_4 and 1.0 M KOH media at different bias voltages.

Acknowledgements
This work was supported by the National Natural Science Foundation of China (21522106, 21971117, 21661023, 21601096, 21802076, 21962013, and 21971129), the Natural Science Foundation of Inner Mongolia Autonomous Region of China (2018BS05007), the Program of Higher-level Talents of IMU (21300-5155105, 21300-5185111, and 21300-5195109), and the Cooperation Project of the State Key Laboratory of Baiyun Obo Rare Earth Resource Research and Comprehensive Utilization (2017Z1950). We also acknowledge the financial support from the 111 Project (B18030) from China, the National Key R&D Program of China (No. 2017YFA0208000), the Open Funds (RERU2019001) of the State Key Laboratory of Rare Earth Resource Utilization and the Functional Research Funds for the Central Universities, Nankai University (ZB19500202).

Author details
[1]School of Chemistry and Chemical Engineering, Inner Mongolia Key Lab of Nanoscience and Nanotechnology, Inner Mongolia Engineering and Technology Research Center for Catalytic Conversion and Utilization of Carbon Resource Molecules, Inner Mongolia University, Hohhot 010021, People's Republic of China. [2]Chemistry and Chemical Engineering Guangdong Laboratory, Shantou 515031, People's Republic of China. [3]Department of Physics, School of Science, Beijing Jiaotong University, Beijing 100044, People's Republic of China. [4]Tianjin Key Lab for Rare Earth Materials and Applications, Center for Rare Earth and Inorganic Functional Materials, School of Materials Science and Engineering & National Institute for Advanced Materials, Nankai University, Tianjin 300350, People's Republic of China

Author contributions
B.L., J.Z., and Y.D. conceived the idea and designed the research. B.C. and Y.C. carried out experiments with the technical support of B.Z. and X.W.; M.H. and R.G. carried out the DFT calculations. B.C. wrote the first manuscript. P.J. and X.S. provided suggestions for analyzing the experiments in the manuscript. All authors contributed to interpreting the results and revising the manuscript.

Conflict of interest
The authors declare that they have no conflict of interest.

Supplementary information is available for this paper at https://doi.org/10.1038/s41427-020-00264-x.

Received: 19 April 2020 Revised: 14 September 2020 Accepted: 5 October 2020.
Published online: 8 January 2021

References

1. Chu, S. & Majumdar, A. Opportunities and challenges for a sustainable energy future. *Nature* **488**, 294–303 (2012).
2. Detchon, R. & Leeuwen, R. V. Bring sustainable energy to the developing world. *Nature* **508**, 309–311 (2014).
3. Bai, S. et al. Surface polarization matters: enhancing the hydrogen-evolution reaction by shrinking Pt shells in Pt-Pd-graphene stack structures. *Angew. Chem. Int. Ed.* **53**, 12120–12124 (2014).
4. Deng, J., Ren, P., Deng, D. & Bao, X. Enhanced electron penetration through an ultrathin graphene layer for highly efficient catalysis of the hydrogen evolution reaction. *Angew. Chem. Int. Ed.* **54**, 2100–2104 (2014).
5. Xiao, F. et al. Phytic acid-guided ultra-thin N,P co-doped carbon coated carbon nanotubes for efficient all-pH electrocatalytic hydrogen evolution. *Nanoscale* **11**, 23027–23034 (2019).
6. Yue, X., Huang, S., Cai, J., Jin, Y. & Shen, P. K. Heteroatoms dual doped porous graphene nanosheets as efficient bifunctional metal-free electrocatalysts for overall water-splitting. *J. Mater. Chem. A* **5**, 7784–7790 (2017).
7. Huang, S. et al. N-, O- and P-doped hollow carbons: Metal-free bifunctional electrocatalysts for hydrogen evolution and oxygen reduction reactions. *Appl. Catal. B* **248**, 239–248 (2019).
8. Tan, X., Tahini, H. A. & Smith, S. C. p-Doped graphene/graphitic carbon nitride hybrid electrocatalysts: unraveling charge transfer mechanisms for enhanced hydrogen evolution reaction performance. *ACS Catal.* **6**, 7071–7077 (2016).
9. Zhu, Y. et al. Structural engineering of 2D nanomaterials for energy storage and catalysis. *Adv. Mater.* **30**, 1706347 (2016).
10. Ekspong, J. et al. Stabilizing active edge sites in semicrystalline molybdenum sulfide by anchorage on nitrogen-doped carbon nanotubes for hydrogen evolution reaction. *Adv. Funct. Mater.* **26**, 6766–6776 (2016).
11. Wang, D. Y. et al. Highly active and stable hybrid catalyst of cobalt-doped FeS_2 nanosheets-carbon nanotubes for hydrogen evolution reaction. *J. Am. Chem. Soc.* **137**, 1587–1592 (2015).
12. Deng, J. et al. High-performance hydrogen evolution electrocatalysis by layer-controlled MoS_2 nanosheets. *Energy Environ. Sci.* **7**, 1919–1923 (2014).
13. Xu, K. et al. Controllable surface reorganization engineering on cobalt phosphide nanowire arrays for efficient alkaline hydrogen evolution reaction. *Adv. Mater.* **30**, 1703322 (2018).
14. Guo, Y. et al. Nanoarchitectonics for transition-metal-sulfide-based electrocatalysts for water splitting. *Adv. Mater.* **31**, 1807134 (2019).
15. Li, S. et al. Metal-organic precursor-derived mesoporous carbon spheres with homogeneously distributed molybdenum carbide/nitride nanoparticles for efficient hydrogen evolution in alkaline media. *Adv. Funct. Mater.* **29**, 1807419 (2019).
16. Chen, Z. et al. Ultrafine Co nanoparticles encapsulated in carbon-nanotubes-grafted graphene sheets as advanced electrocatalysts for the hydrogen evolution reaction. *Adv. Mater.* **30**, 1802011 (2018).
17. Zhang, L., Xiao, J., Wang, H. & Shao, M. Carbon-based electrocatalysts for hydrogen and oxygen evolution reactions. *ACS Catal.* **7**, 7855–7865 (2017).
18. Ma, Y.-Y. et al. Highly efficient hydrogen evolution from seawater by a low-cost and stable CoMoP@C electrocatalyst superior to Pt/C. *Energy Environ. Sci.* **10**, 788–798 (2017).
19. Chen, Z. et al. Tailoring the d-band centers enables Co_4N nanosheets to be highly active for hydrogen evolution catalysis. *Angew. Chem. Int. Ed.* **57**, 5076–5080 (2018).
20. Zhang, Y. et al. Rapid synthesis of cobalt nitride nanowires: highly efficient and low-cost catalysts for oxygen evolution. *Angew. Chem. Int. Ed.* **55**, 8670–8674 (2016).
21. Guo, X. et al. Single-crystalline organic-inorganic layered cobalt hydroxide nanofibers: facile synthesis, characterization, and reversible water-induced structural conversion. *Inorg. Chem.* **53**, 12841–12847 (2014).
22. Zhang, E. et al. Bismuth single atoms resulting from transformation of metal-organic frameworks and their use as electrocatalysts for CO_2 reduction. *J. Am. Chem. Soc.* **141**, 16569–16573 (2019).
23. Varga, T. et al. Co_4N/nitrogen-doped graphene: a non-noble metal oxygen reduction electrocatalyst for alkaline fuel cells. *Appl. Catal. B* **237**, 826–834 (2018).
24. Fei, H. et al. Atomic cobalt on nitrogen-doped graphene for hydrogen generation. *Nat. Commun.* **6**, 8668 (2015).
25. Yoon, K. R. et al. Brush-like cobalt nitride anchored carbon nanofiber membrane: current collector-catalyst integrated cathode for long cycle Li-O_2 batteries. *ACS Nano* **12**, 128–139 (2018).

26. Han, X. et al. Ultrafine Pt nanoparticle-decorated pyrite-type CoS_2 nanosheet arrays coated on carbon cloth as a bifunctional electrode for overall water splitting. *Adv. Energy Mater.* **8**, 1800935 (2018).
27. Cao, B., Veith, G. M., Neuefeind, J. C., Adzic, R. R. & Khalifah, P. G. Mixed close-packed cobalt molybdenum nitrides as non-noble metal electrocatalysts for the hydrogen evolution reaction. *J. Am. Chem. Soc.* **135**, 19186–19192 (2013).
28. Yin, J. et al. Ni-C-N nanosheets as catalyst for hydrogen evolution reaction. *J. Am. Chem. Soc.* **138**, 14546–14549 (2016).
29. Feng, J. X., Tong, S. Y., Tong, Y. X. & Li, G. R. Pt-like hydrogen evolution electrocatalysis on PANI/CoP hybrid nanowires by weakening the shackles of hydrogen ions on the surfaces of catalysts. *J. Am. Chem. Soc.* **140**, 5118–5126 (2018).
30. Pan, Y. et al. Core–shell ZIF-8@ ZIF-67-derived CoP nanoparticle-embedded N-doped carbon nanotube hollow polyhedron for efficient overall water splitting. *J. Am. Chem. Soc.* **140**, 2610–2618 (2018).
31. Chen, Y. et al. Hollow carbon-nanotube/carbon-nanofiber hybrid anodes for Li-ion batteries. *J. Am. Chem. Soc.* **135**, 16280–16283 (2013).
32. Zhu, Y. et al. A seamless three-dimensional carbon nanotube graphene hybrid material. *Nat. Commun.* **3**, 1225 (2012).
33. Cui, X., Ren, P., Deng, D., Deng, J. & Bao, X. Single layer graphene encapsulating non-precious metals as high-performance electrocatalysts for water oxidation. *Energy Environ. Sci.* **9**, 123–129 (2016).
34. Peng, S. et al. Cobalt sulfide nanosheet/graphene/carbon nanotube nanocomposites as flexible electrodes for hydrogen evolution. *Angew. Chem. Int. Ed.* **53**, 12594–12599 (2014).
35. Staszak-Jirkovsky, J. et al. Design of active and stable Co–Mo–S_x chalcogels as pH-universal catalysts for the hydrogen evolution reaction. *Nat. Mater.* **15**, 197–203 (2016).
36. Chen, G.-F. et al. Efficient and stable bifunctional electrocatalysts Ni/Ni_xM_y (M = P, S) for overall water splitting. *Adv. Funct. Mater.* **26**, 3314–3323 (2016).
37. Lukowski, M. A. et al. Enhanced hydrogen evolution catalysis from chemically exfoliated metallic MoS_2 nanosheets. *J. Am. Chem. Soc.* **135**, 10274–10277 (2013).
38. Wang, X.-D. et al. Novel porous molybdenum tungsten phosphide hybrid nanosheets on carbon cloth for efficient hydrogen evolution. *Energy Environ. Sci.* **9**, 1468–1475 (2016).
39. Liu, Y. et al. Coupling Mo_2C with nitrogen-rich nanocarbon leads to efficient hydrogen-evolution electrocatalytic sites. *Angew. Chem. Int. Ed.* **54**, 10752–10757 (2015).
40. Gao, R. et al. Ultradispersed nickel phosphide on phosphorus-doped carbon with tailored d-band center for efficient and chemoselective hydrogenation of nitroarenes. *ACS Catal.* **8**, 8420–8429 (2018).